J Adv Ceram

Research Article

Dual rare-earth modification and interface engineering in SiC-based heterostructures for multi-frequency electromagnetic wave absorption

Jingyi Xu†, Zhanming Wu†, Yunan Tan, Xiaojun Zeng✉

Cite this article: Xu JY, Wu ZM, Tan YN, et al. *J Adv Ceram* 2026, **15**(7): 9221325. https://doi.org/10.26599/JAC.2026.9221325

ABSTRACT: The escalating complexity of the electromagnetic environment calls for advanced electromagnetic wave (EMW) absorption materials capable of efficient multi-frequency attenuation. Silicon carbide (SiC) is a promising dielectric candidate but is hindered by intrinsic impedance mismatch and limited polarization loss. Herein, we report a novel ternary heterostructure absorber consisting of SiC nanowires synergistically coupled with dual rare-earth silicides (Ce_5Si_4 and Pr_5Si_4) fabricated via a combined magnesiothermic and carbothermal reduction process using an MFI-type zeolite precursor. This unique architecture creates an intricate porous network featuring abundant multiple heterogeneous interfaces (SiC/Ce_5Si_4, SiC/Pr_5Si_4, and Ce_5Si_4/Pr_5Si_4). The simultaneous incorporation of Ce and Pr optimizes the complex permittivity for impedance matching and induces intense multi-interfacial polarization relaxation. Consequently, the designed composite achieves efficient and strong EMW absorption performance in the C-band (4.30 GHz), X-band (8.24 GHz), and Ku-band (16.51 GHz), demonstrating remarkable multi-frequency point absorption performance. Radar cross-section (RCS) simulations further demonstrate its significant stealth capability, highlighting the potential of dual rare-earth synergistic engineering. This work provides a pioneering strategy for designing high-performance, multi-frequency SiC-based absorbers through the construction of ternary rare-earth silicide heterostructures.

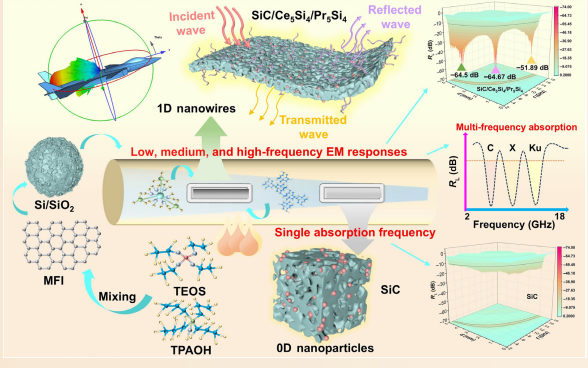

KEYWORDS: silicon carbide (SiC); dual rare-earth; interfacial polarization; multi-frequency absorption; electromagnetic wave absorption

1 Introduction

With the rapid development of the modern electronic information industry, the interference and pollution problems caused by the increasingly complex electromagnetic environment can no longer be ignored [1–3]. High-intensity and multi-frequency electromagnetic radiation not only seriously endangers the stable operation of electronic equipment and information security but also poses a potential threat to biological health [4–6]. Therefore, the development of high-performance electromagnetic wave (EMW) absorption materials with strong multi-band absorption capabilities covering low, medium, and high frequencies has become a key research topic in the fields of frontier materials science and electromagnetic protection [7,8]. An ideal absorber should achieve efficient electromagnetic energy dissipation over a wide frequency range (e.g., covering the low-, mid-, and high-frequency segments of the microwave band) while possessing excellent impedance matching characteristics to meet the urgent demands for electromagnetic compatibility and radiation protection in multi-frequency application scenarios [9,10].

Silicon carbide (SiC), as a typical wide-bandgap semiconductor material, exhibits good chemical stability, high-temperature resistance, and tunable dielectric properties, making it a promising next-generation dielectric absorber [11]. However, intrinsic SiC suffers from a relatively high dielectric constant, which easily leads to impedance mismatch at the air–material interface [12]. Additionally, its limited polarization loss capability makes it difficult to achieve efficient EMW dissipation across multiple frequency bands [13].

To overcome these bottlenecks, researchers have commonly adopted strategies such as constructing heterostructures, introducing porous morphologies, compositing magnetic

† Jingyi Xu and Zhanming Wu contributed equally to this work.

Jiangxi Key Laboratory of Advanced Ceramic Materials, School of Materials Science and Engineering, Jingdezhen Ceramic University, Jingdezhen 333403, China.

✉ Corresponding author. E-mail: zengxiaojun@jci.edu.cn

Received: March 18, 2026; Revised: April 28, 2026; Accepted: May 20, 2026

components, or performing element doping to optimize the electromagnetic parameters of materials [14]. Among these, the construction of heterogeneous interfaces is regarded as an effective way to enhance interfacial polarization and improve polarization loss [15]. In addition, rare-earth elements, with their unique 4f electron shell structures and variable valence states, have demonstrated significant advantages in regulating the electronic structure of materials, introducing defect polarization, and enhancing interface interactions [16]. Previous works have shown that the incorporation of rare-earth elements into the SiC system can form rare-earth silicides (e.g., CeSi), which exhibit differences in electrical conductivity and dielectric properties from SiC. These differences can induce intense charge accumulation and dipole polarization at the interfaces, thereby significantly enhancing the dielectric loss capability of the absorber [17]. However, existing works have focused on the doping effect of a single rare-earth element, and systematic and in-depth research on the regulatory mechanism underlying the synergistic effect of dual rare-earth elements on the heterostructure construction, interfacial polarization behavior, and multi-band absorption performance of SiC-based materials is still lacking.

Based on this, this work designed and successfully fabricated a ternary SiC/Ce_5Si_4/Pr_5Si_4 heterostructure. All-silica MFI-type zeolites were used as the silicon source and precursor, and combined with magnesiothermic and carbothermal reduction processes, dual rare-earth nitrates (Ce and Pr) were simultaneously introduced. Under high-temperature conditions, Ce_5Si_4 and Pr_5Si_4 species were formed, and SiC nanowires were catalytically grown, ultimately constructing a porous network structure with abundant multiple heterogeneous interfaces (SiC/Ce_5Si_4, SiC/Pr_5Si_4, and Ce_5Si_4/Pr_5Si_4). The results indicate that Ce and Pr not only effectively regulated the real and imaginary parts of the dielectric constant of the composite but also induced intense interfacial polarization relaxation. Consequently, efficient multi-band EMW absorption was achieved in the C-band (4.3 GHz), X-band (8.24 GHz), and Ku-band (16.51 GHz). Radar cross-section (RCS) simulations further verified the potential of this composite in aerospace stealth applications. This work provides a new idea and experimental basis for the design of high-performance, multi-frequency SiC-based absorbers using dual rare-earth elements.

2 Experimental methods

2.1 Chemicals

Tetraethyl orthosilicate (TEOS; Sinopharm Chemical Reagent Co., Ltd.), tetrapropyl ammonium hydroxide (TPAOH; 25 wt%, Anhui Senrise Technologies Co., Ltd.), magnesium powder (Mg; 99.5%, Tianjin Damao Chemical Reagent Factory), sucrose ($C_{12}H_{22}O_{11}$; 99%, Sinopharm Chemical Reagent Co., Ltd.), hydrochloric acid (HCl; 36 wt%, Sinopharm Chemical Reagent Co., Ltd.), and $Ce(NO_3)_3{\cdot}6H_2O$ and $Pr(NO_3)_3{\cdot}6H_2O$ (99%, Shanghai Macklin Biochemical Technology Co., Ltd.) were used directly.

2.2 Synthesis of all-silica MFI-type zeolite

TEOS (6.93 g), TPAOH (10.56 g), and deionized (DI) water (15.84 g) were mixed and stirred continuously for 8 h at room temperature. The mixture was then transferred into a 100 mL autoclave and reacted at 180 °C for 48 h, followed by cooling to room temperature. The product was washed repeatedly with deionized water and absolute ethanol and collected by centrifugation until the supernatant reached neutral pH. The collected solid was dried at 100 °C for 12 h and finally calcined in a muffle furnace at 550 °C for 4 h at a heating rate of 2 °C·min^{-1} to obtain the all-silica MFI-type zeolite.

2.3 Synthesis of Si/SiO_2 powder

All-silica MFI-type zeolite (250 mg) and magnesium powder (250 mg) were thoroughly ground together for 45 min. The mixture was then heated to 700 °C at a rate of 5 °C·min^{-1} under an argon atmosphere, maintained at this temperature for 5 h, and allowed to cool naturally. The resulting product was stirred in 20 mL of a hydrochloric acid solution (1 M) for 24 h, followed by repeated washing and centrifugation. Finally, the material was dried in a vacuum oven at 80 °C for 12 h to yield Si/SiO_2 powder.

2.4 Synthesis of SiC/Ce_5Si_4/Pr_5Si_4 heterostructures

First, 0.237 g of sucrose and 0.1 g of Si/SiO_2 powder were dissolved in 10 mL of deionized water. Subsequently, 15 mg of $Ce(NO_3)_3{\cdot}6H_2O$ and 15 mg of $Pr(NO_3)_3{\cdot}6H_2O$ were added to the solution, which was then sonicated for 10 min and stirred at room temperature for 3 h. The mixture was freeze-dried for 48 h to obtain a solid precursor. The precursor was heat-treated using a stepwise procedure: It was first heated to 800 °C at a rate of 2 °C·min^{-1} and held for 2 h, then further heated to 1400 °C at a rate of 5 °C·min^{-1} and maintained for another 2 h. The final product was denoted as SiC/Ce_5Si_4/Pr_5Si_4.

To investigate the influence of rare-earth modification on the EMW absorption performance, comparative experiments were carried out under identical synthetic conditions: one with no rare earth, one with $Ce(NO_3)_3{\cdot}6H_2O$ only, and one with both $Ce(NO_3)_3{\cdot}6H_2O$ and $Pr(NO_3)_3{\cdot}6H_2O$ (the previously described system). The resulting samples were denoted as SiC, SiC/Ce_5Si_4, and SiC/Ce_5Si_4/Pr_5Si_4, respectively.

2.5 Characterizations

The morphology and microstructure of the samples were examined using a field-emission scanning electron microscope (FE-SEM; SU-8010, Hitachi, Japan) and a transmission electron microscope (TEM; JEM-F200, JEOL, Japan). Elemental composition and distribution were analyzed via an energy-dispersive X-ray spectrometer (EDS) attached to the FE-SEM. Phase identification was performed using an X-ray diffractometer (XRD; D8 Advance, Bruker, Germany) with Cu Kα radiation (λ = 0.15406 nm) operated at 40 kV and 30 mA. Chemical states and surface composition were investigated using an X-ray photoelectron spectrometer (XPS; Thermo Escalab 250Xi, USA). The Brunauer–Emmett–Teller (BET) specific surface area and pore size distributions of SiC and SiC/Ce_5Si_4/Pr_5Si_4 were obtained using nitrogen adsorption–desorption isotherm analysis with a Micromeritics-specific surface area analyzer (ASAP2020M, Micromeritics, USA).

2.6 Electromagnetic parameter measurement

The electromagnetic parameters of the samples were measured in the frequency range of 2–18 GHz using a vector network analyzer (VNA, Ceyear 3656D, China). To evaluate the EMW absorption performance, each sample was uniformly mixed with paraffin at a mass ratio of 5 : 5 and pressed into toroidal-shaped samples with an inner diameter of 3.04 mm and an outer diameter of 7.00 mm. The reflection loss (R_L), a key indicator of the EMW attenuation ability, was calculated according to standard transmission-line theory, as given by Eqs. (1) and (2) [18,19].

$$Z_{in} = Z_0(\mu_r/\varepsilon_r)^{1/2}\tanh[j(2\pi fd/c)(\mu_r\varepsilon_r)^{1/2}] \quad (1)$$

$$R_L = 20\log_{10}|(Z_{in}-Z_0)/(Z_{in}+Z_0)| \quad (2)$$

where Z_{in} and Z_0 are the input impedance and free-space impedance, respectively. ε_r, μ_r, f, d, and c are the complex permittivity, complex permeability, frequency, thickness of the sample, and velocity of light, respectively.

3 Results and discussion

Figure 1 illustrates the synthesis route of the SiC/Ce_5Si_4/Pr_5Si_4 heterostructures. Initially, an all-silica zeolite with MFI topology was hydrothermally synthesized using TEOS as the silicon source and TPAOH as the structure-directing agent. This zeolite not only provides silicon, but its ordered porous structure also helps to inherit porosity in the final product, thereby extending the EMW propagation path and enhancing multiple scattering and energy dissipation [20]. Subsequently, the all-silica zeolite was ground and mixed with magnesium powder, followed by magnesiothermic reduction to yield Si/SiO_2 powder with abundant porous structures [21]. Next, the Si/SiO_2 powder was uniformly mixed with a carbon source (sucrose) and rare-earth nitrates ($Ce(NO_3)_3{\cdot}6H_2O$ and $Pr(NO_3)_3{\cdot}6H_2O$), followed by freeze drying. The introduction of rare-earth salts aims to generate rare-earth silicides (Ce_5Si_4 and Pr_5Si_4) via reaction with silicon at high temperature and to promote the growth of one-dimensional (1D) SiC. These silicides exhibit significant differences in electrical properties compared with SiC, creating conditions for constructing multiple heterointerfaces and inducing strong interfacial polarization. Finally, the freeze-dried precursor was subjected to stepwise heat treatment under an inert atmosphere. During heating, the rare-earth elements are reduced to active rare-earth species under the carbon-reducing atmosphere. Simultaneously, Si/SiO_2 reacts with carbon to generate gaseous SiO. Active rare-earth species with gaseous SiO or solid silicon at approximately 1200–1250 °C form Ce_5Si_4 and Pr_5Si_4. Since both silicides have melting points of approximately 1250 °C, they form molten droplets upon reaching the final temperature of 1400 °C and catalyze the growth of SiC nanowires via the vapor–liquid–solid (VLS) mechanism [22]. Upon cooling, the droplets solidify into crystalline Ce_5Si_4 and Pr_5Si_4, which are nanoscopically integrated with SiC, yielding abundant heterointerfaces. The abundant heterointerfaces between SiC and the two rare-earth silicides introduce remarkable interfacial polarization loss, endowing the SiC/Ce_5Si_4/Pr_5Si_4 composite with excellent multi-frequency EMW absorption performance, as illustrated by the pie and bar charts.

The phase compositions of SiC, SiC/Ce_5Si_4, and SiC/Ce_5Si_4/Pr_5Si_4 composites were analyzed using XRD. As shown in Fig. 2(a), all samples exhibit well-defined diffraction peaks at 2θ = 35.7°, 60.2°, and 71.8°, which correspond to the (111), (220), and (311) crystal planes of β-SiC (PDF#29-1129), respectively, confirming the successful synthesis of a well-crystallized β-SiC structure [23]. In the XRD pattern of the SiC/Ce_5Si_4 composite, in addition to the characteristic peaks of SiC, diffraction signals matching the Ce_5Si_4 phase (PDF#97-016-7179) can be identified [22]. For the ternary SiC/Ce_5Si_4/Pr_5Si_4 composite, diffraction peaks attributable to the Pr_5Si_4 phase (PDF#97-009-8352) further appear, verifying the successful incorporation of Pr_5Si_4. Notably, with the formation of the Ce_5Si_4 and Pr_5Si_4 phases, the intensity of the main SiC diffraction peaks only shows a slight reduction, while their positions and shapes remain unchanged. This indicates that the introduction of rare-earth elements did not change the crystal structure of β-SiC.

The nitrogen adsorption–desorption isotherms (Fig. 2(b)) reveal that the adsorbed volume is relatively low at low relative pressures ($P/P_0 < 0.1$) and gradually increases with rising pressure, exhibiting a distinct upward trend in the medium-to-high pressure region ($P/P_0 \approx 0.4$–0.9). Both isotherms conform to

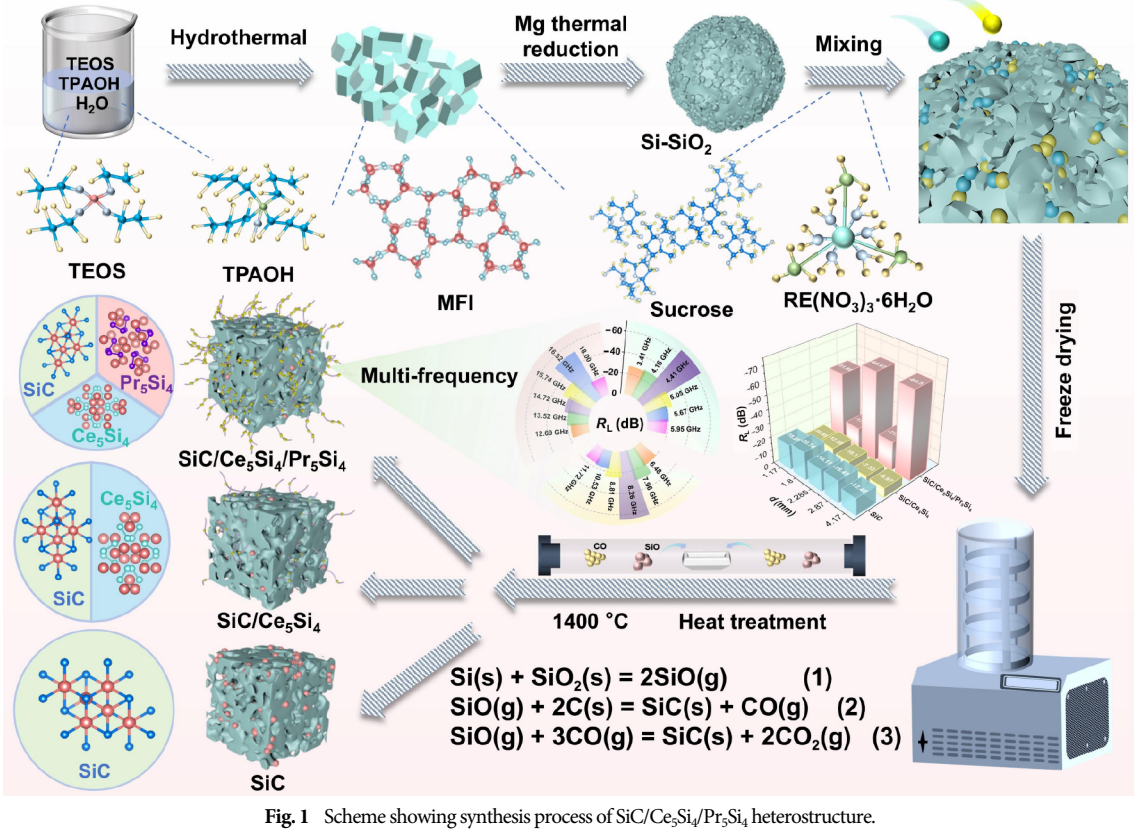

Fig. 1 Scheme showing synthesis process of SiC/Ce_5Si_4/Pr_5Si_4 heterostructure.

清華大学出版社 Tsinghua University Press | SciOpen

type IV characteristics and display an H3-type hysteresis loop, indicating that the materials are predominantly mesoporous [24]. The specific surface areas of SiC and SiC/Ce_5Si_4/Pr_5Si_4 are 46.4 and 93.5 $m^2 \cdot g^{-1}$, respectively. The SiC/Ce_5Si_4/Pr_5Si_4 composite exhibits significantly higher adsorbed volumes across the entire pressure range than pure SiC, indicating a more developed pore structure and a larger total pore volume. The corresponding pore size distribution curves (Fig. 2(c)) further demonstrate a bimodal distribution of SiC/Ce_5Si_4/Pr_5Si_4, with distinct peaks located at approximately 3.92 and 31.14 nm. This porous network provides abundant scattering paths and heterogeneous interfaces, which are crucial for multi-band EMW absorption [25].

XPS was employed to analyze the surface chemical states of the samples, aiming to elucidate the elemental composition and key chemical bonding configurations in the SiC, SiC/Ce_5Si_4, and SiC/Ce_5Si_4/Pr_5Si_4 composites. The relevant results are presented in Figs. 2(d)–2(i). The XPS survey spectrum (Fig. 2(d)) clearly shows the characteristic peaks of Si, C, Pr, Ce, O, and N, confirming the presence of the targeted elements in the designed composites. The high-resolution XPS spectra of Pr 3d and Ce 3d (Figs. 2(e) and 2(f)) display characteristic features of a mixed valence state involving both Pr^{3+}/Pr^{4+} and Ce^{3+}/Ce^{4+}. This mixed valency is typically associated with localized charge inhomogeneity, which can promote dipole polarization and interface relaxation, thereby enhancing EMW dissipation capabilities [26]. The high-resolution XPS spectrum of Si 2p (Fig. 2(g)) was deconvoluted into two main components. The peak located at a binding energy of 101.4 eV is assigned to the Si–C bond, corresponding to the formation of the SiC lattice [27]. The peak at 102.9 eV is attributed to the Si–O bond, indicating the presence of a small amount of residual silicon oxide in the material. The high-resolution XPS spectra of C 1s (Fig. 2(h)) could be deconvoluted into three peaks. The peak at 283.3 eV is attributed to the C–Si bond, further confirming the successful construction of the SiC crystalline phase. The intense peak at 284.8 eV corresponds to C–C bonds, indicating the existence of graphitized carbon regions within the material, which contribute to conduction loss. The weaker peak at 285.6 eV originates from C–O bonds, likely related to surface adsorbed oxygen or precursor residues [28]. The high-resolution XPS spectrum of N 1s (Fig. 2(i)) reveals two fitted peaks at 397.9 and 400.2 eV, corresponding to pyridinic nitrogen and graphitic nitrogen, respectively [29]. Furthermore, the high-resolution XPS spectrum of O 1s (Fig. S1 in the Electronic Supplementary Material (ESM)) shows identifiable O–Si components, indicating that some silicon and carbon species are in an oxidized state [30]. In summary, the chemical shifts and multi-component bonding

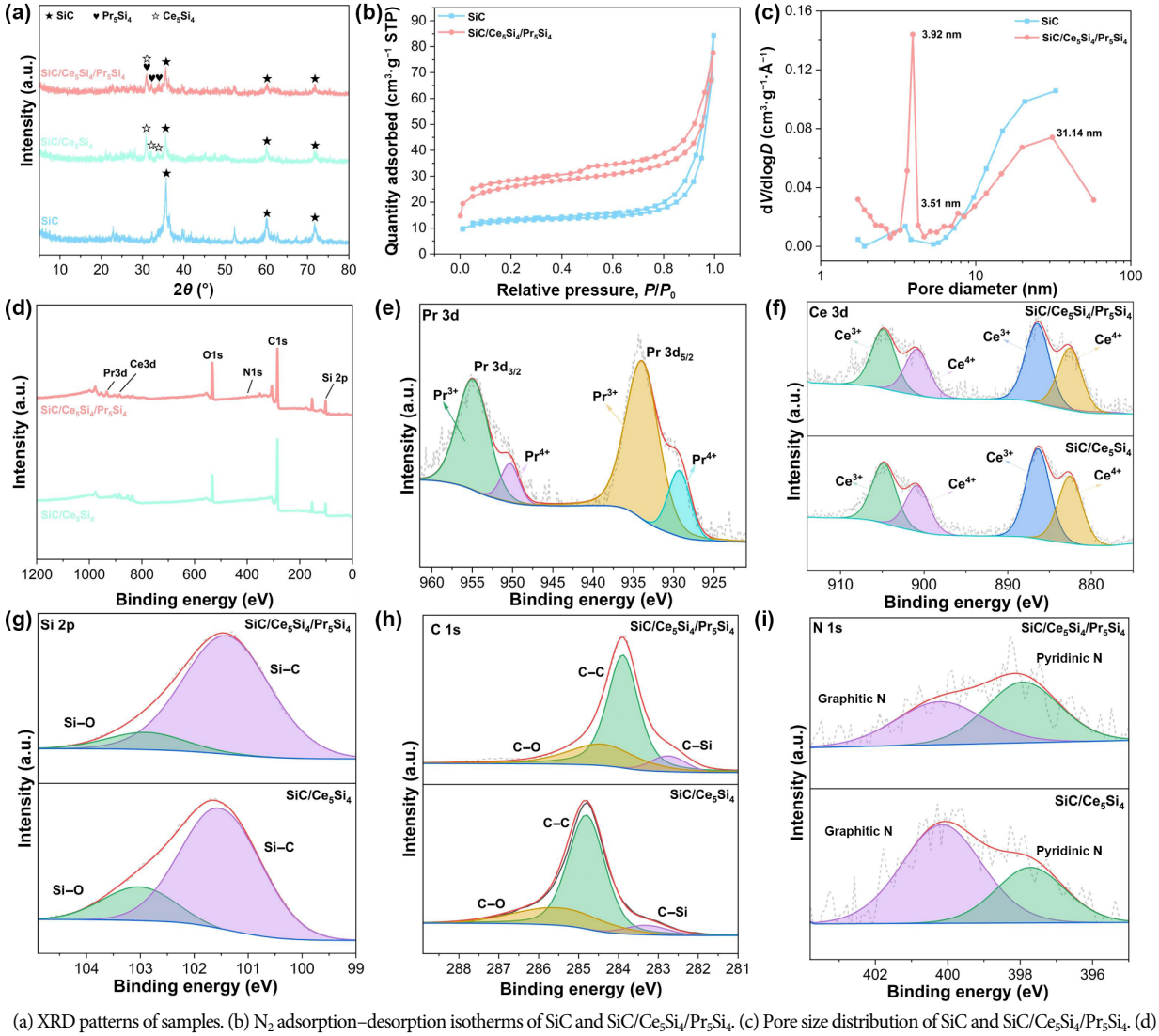

Fig. 2 (a) XRD patterns of samples. (b) N_2 adsorption–desorption isotherms of SiC and SiC/Ce_5Si_4/Pr_5Si_4. (c) Pore size distribution of SiC and SiC/Ce_5Si_4/Pr_5Si_4. (d) XPS survey spectra of SiC/Ce_5Si_4 and SiC/Ce_5Si_4/Pr_5Si_4. High-resolution XPS spectra of (e) Pr 3d, (f) Ce 3d, (g) Si 2p, (h) C 1s, and (i) N 1s for SiC/Ce_5Si_4 and SiC/Ce_5Si_4/Pr_5Si_4.

features common in the XPS spectra indicate that the introduction of dual rare-earth elements (Ce/Pr) significantly modulates the chemical environment of the material [31].

The microstructural morphology and composition of the samples were systematically characterized using FE-SEM and TEM, with the results presented in Fig. 3. The Si/SiO_2 powder obtained via magnesiothermic reduction (Fig. 3(a) and Fig. S2 in the ESM) exhibits a porous and interconnected composite architecture consisting of rough-surfaced nanoparticles and their aggregates. This high specific surface area and porous morphology facilitate the reduction of the SiC formation temperature during the subsequent carbothermal reduction process. After calcination and carbonization under an argon atmosphere, the pure SiC sample is composed of numerous nanoparticles, which undergo close packing and agglomeration due to strong interparticle interactions (Fig. 3(b) and Fig. S3 in the ESM). The introduction of Ce leads to a significant transformation in the morphology of the material. As shown in Fig. 3(c) and Fig. S4 in the ESM, a large quantity of 1D SiC nanowires, with lengths reaching several micrometers, along with partially unconverted particles, collectively form a three-dimensional (3D) network structure. This morphological evolution indicates that Ce alters the growth mechanism of SiC, shifting from isotropic particle accumulation to anisotropic axial growth. Upon further incorporation of Pr, the sample (Fig. 3(d)) still predominantly consists of nanowires, suggesting that the dual rare-earth elements synergistically promote the VLS growth process. During this process, the rare-earth nitrates are reduced at high temperatures and form low-melting-point eutectic droplets with silicon. These droplets act as catalytic sites, adsorbing gaseous SiO and carbon sources; upon supersaturation, SiC crystals precipitate, driving nanowire growth. The high specific surface area, abundant surface dangling bonds, and crystal defects such as stacking faults introduced during the growth of the nanowires, together with the resulting heterointerfaces, collectively enhance interfacial polarization and dipole polarization losses [22]. The EDS elemental mapping results (Fig. 3(e) and Fig. S5 in the ESM) reveal a uniform distribution of Ce and Pr within the SiC matrix, confirming the successful incorporation of rare-earth elements. TEM images (Fig. 3(f) and Figs. S6(a) and S6(b) in the ESM) further demonstrate that $SiC/Ce_5Si_4/Pr_5Si_4$ consists of SiC nanowires and nanoparticles attached to them, featuring abundant interfaces. HRTEM analysis (Figs. 3(g)–3(i)) reveals lattice fringe spacings of 0.25 and 0.15 nm in the nanowire and particle regions, corresponding to the (111) and (220) planes of SiC, respectively [32]. Furthermore, the elemental distribution maps in Fig. 3(j) and Fig. S7 in the ESM show that Si and C are densely dispersed throughout the nanowires, whereas Ce and Pr are primarily localized in the particulate regions, clearly revealing the spatial chemical distribution characteristics of this heterostructure.

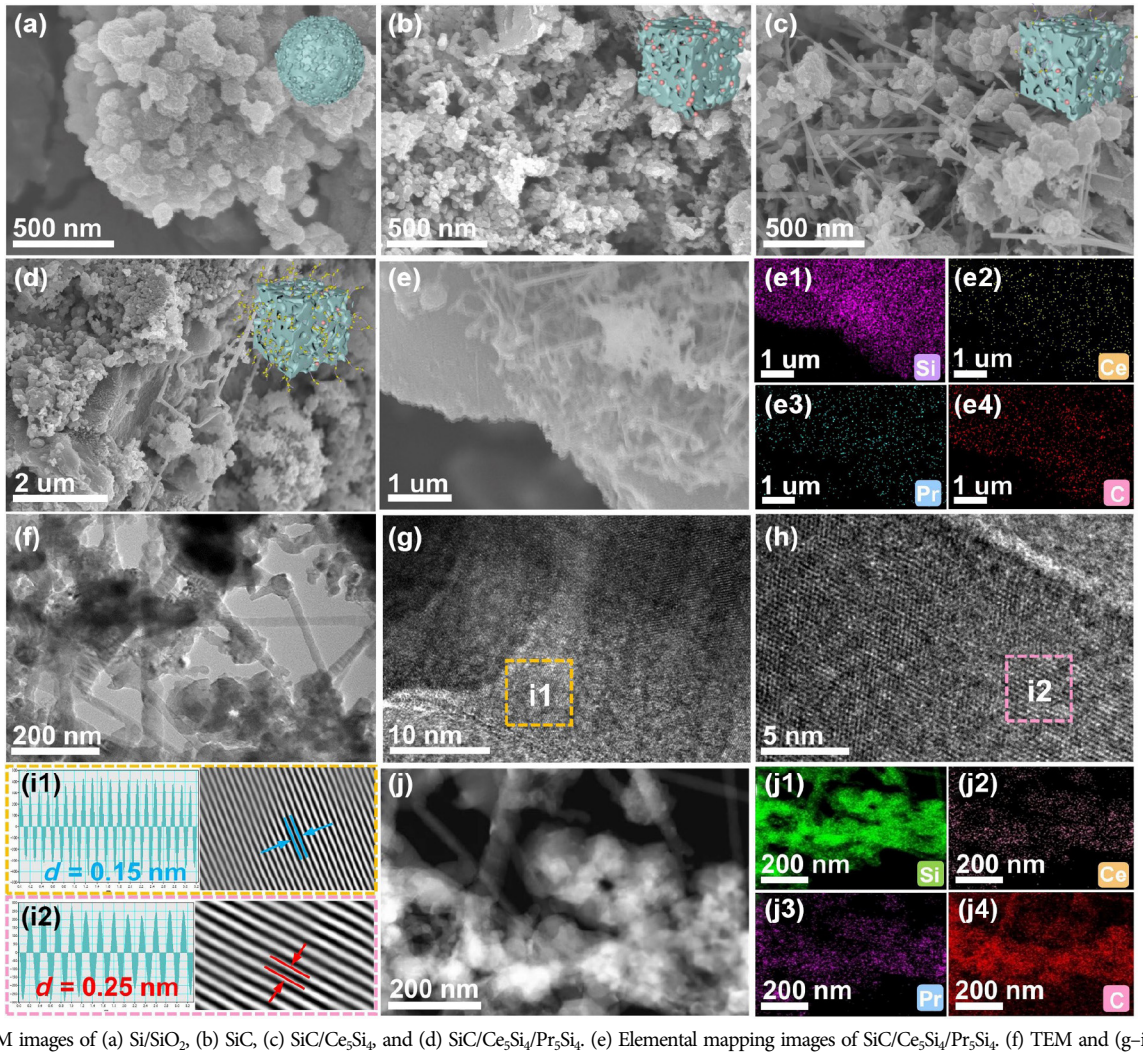

Fig. 3 SEM images of (a) Si/SiO_2, (b) SiC, (c) SiC/Ce_5Si_4, and (d) $SiC/Ce_5Si_4/Pr_5Si_4$. (e) Elemental mapping images of $SiC/Ce_5Si_4/Pr_5Si_4$. (f) TEM and (g–i) HRTEM images of $SiC/Ce_5Si_4/Pr_5Si_4$. The interplanar spacing in the (i1) i1 region of (g) and the i2 region of (h). (j) Elemental mapping images of $SiC/Ce_5Si_4/Pr_5Si_4$.

Figures 4(a)–4(f) present the two-dimensional (2D) and 3D distributions of the reflection loss (R_L) of the samples as functions of frequency and thickness. As shown in Fig. 4(a), intrinsic SiC exhibits weak EMW absorption performance. At a thickness of 1.8 mm, its minimum R_L is −20.74 dB at a frequency of 11.78 GHz. This is primarily attributed to the limited intrinsic dielectric loss capability of SiC, which restricts its efficiency in dissipating electromagnetic energy. When the matching thickness is 1.11 mm, its effective absorption bandwidth (EAB; $R_L \leq -10$ dB) is 3.73 GHz (Fig. 4(d)). In contrast, after introducing the single rare-earth element Ce, despite the formation of a SiC/Ce_5Si_4 heterostructure via the reaction between Ce and Si, the EMW absorption performance of the material did not improve significantly. At a thickness of 1.685 mm, an R_L of only −12.88 dB was achieved at 9.66 GHz, and the EAB narrowed to 1.9 GHz (Figs. 4(b) and 4(e)). This result can be attributed to the imbalance between the real and imaginary parts of the permittivity induced by single rare-earth doping, which deteriorates the impedance matching condition and consequently weakens the incident wave coupling and dissipation capability. Notably, when Ce and Pr were co-introduced, the prepared SiC/Ce_5Si_4/Pr_5Si_4 composite demonstrated significantly enhanced multi-band EMW absorption performance. This heterostructure achieved R_L values of −51.89, −64.67, and −64.5 dB in the Ku-band (16.51 GHz), X-band (8.24 GHz), and C-band (4.3 GHz), with corresponding matching thicknesses of 1.17, 2.29, and 4.17 mm, respectively (Fig. 4(c)). Furthermore, at a thickness of 1.23 mm, its EAB could reach 3.81 GHz (Fig. 4(f)). This excellent multi-frequency absorption characteristic mainly originates from the polarization relaxation effects induced by the multiple heterointerfaces within the material [33]. In the SiC/Ce_5Si_4/Pr_5Si_4 composite, a substantial number of heterointerfaces are formed among Ce_5Si_4, Pr_5Si_4, and SiC. Under an alternating electromagnetic field, these interfaces generate significant interfacial polarization, thereby enhancing the dielectric loss capability of the material and ultimately enabling efficient multi-frequency EMW absorption [34]. Figure 4(g) schematically illustrates the structural evolution during synthesis using Si/SiO_2 as the precursor through freeze-drying and carbothermal reduction processes, visually revealing the mechanism of gradually enhanced polarization loss during material preparation. Under the synergistic effect of the dual rare-earth elements, the composite ultimately forms abundant heterointerfaces, further enhancing its EMW dissipation performance.

Figures 5(a)–5(c) show the frequency dependence of the real part (ε') and imaginary part (ε'') of the complex permittivity and the dielectric loss tangent ($\tan\delta_e = \varepsilon''/\varepsilon'$) for the samples in the frequency range of 2–18 GHz. Both pure SiC and SiC/Ce_5Si_4 exhibit relatively high values of ε', ε'', and $\tan\delta_e$, indicating their strong polarization and conduction loss capabilities [35]. However, the high permittivity simultaneously leads to a significant impedance mismatch with free space, causing most of

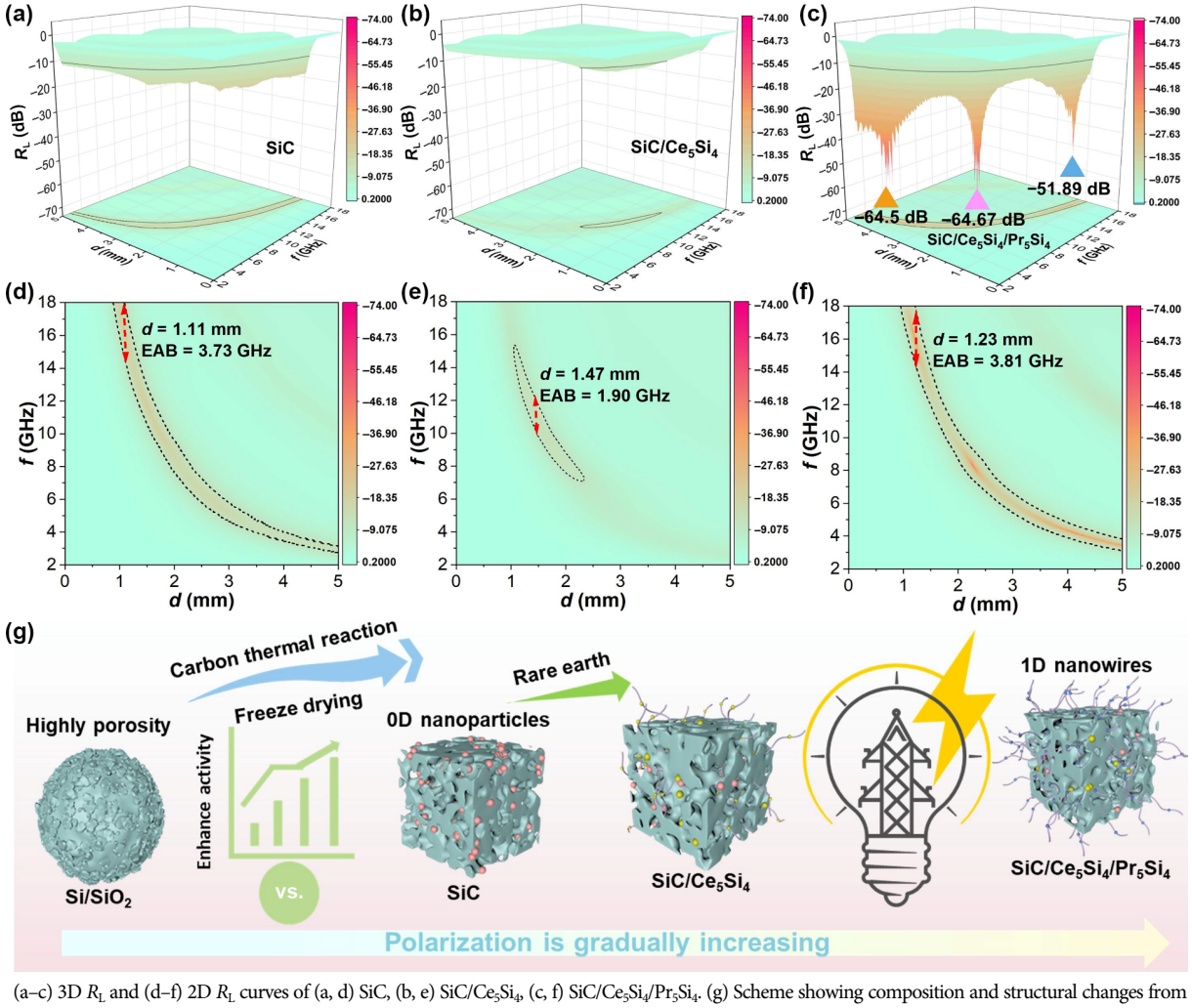

Fig. 4 (a–c) 3D R_L and (d–f) 2D R_L curves of (a, d) SiC, (b, e) SiC/Ce_5Si_4, (c, f) SiC/Ce_5Si_4/Pr_5Si_4. (g) Scheme showing composition and structural changes from SiC to SiC/Ce_5Si_4/Pr_5Si_4.

the incident EMW to be reflected at the material surface and hindering their penetration into the interior for effective dissipation. Consequently, their practical absorption performance is limited [36]. According to the relation of $\varepsilon'' \approx \sigma/(2\pi\varepsilon_0 f)$, the excessively high electrical conductivity (σ) is the primary cause of the significant increase in ε'', which further aggravates the impedance mismatch [37]. Notably, when both Ce and Pr are introduced to form SiC/Ce_5Si_4/Pr_5Si_4, the ε', ε'', and $\tan\delta_e$ values decrease significantly and fall into a moderate range. This regulation of the dielectric parameters effectively alleviates impedance mismatch, allowing more EMW to enter the material interior, thereby laying a critical foundation for achieving excellent EMW absorption performance [38]. In addition, the real part (μ') and imaginary part (μ'') of the complex permeability and the magnetic loss tangent ($\tan\delta_\mu$) spectra of the samples are provided in Figs. S8–S10 in the ESM. All samples show distinct magnetic resonance peaks in the low-frequency region (Fig. S10 in the ESM), originating from natural resonance behavior within the materials [39]. However, across the entire tested frequency range, the $\tan\delta_e$ values of all samples are significantly higher than their corresponding $\tan\delta_\mu$ values. This indicates that dielectric loss is the dominant electromagnetic energy dissipation mechanism in the present system, with magnetic loss serving a supplementary role [40].

According to Debye relaxation theory, dielectric loss can be further decomposed into polarization loss and conduction loss, with detailed procedures provided in Eqs. (S1) and (S2) in the ESM [41]. Based on the analysis of the imaginary part of the complex permittivity, we calculated and separated their respective contributions (labeled as polarization loss (ε_p'') and conduction loss (ε_c''), respectively), with the results shown in Figs. 5(d) and 5(e). The result indicates that across the entire tested frequency range, the contribution of polarization loss exceeds that of conduction loss for all samples, confirming that polarization relaxation is the core mechanism dominating electromagnetic energy dissipation, although a contribution from conduction loss persists in the low-frequency region. Figure 5(f) specifically displays the comparison between the total dielectric loss and its polarization loss component for the SiC/Ce_5Si_4/Pr_5Si_4 composite. Multiple distinct polarization loss peaks can be clearly observed in the low-, mid-, and high-frequency regions, confirming the significant polarization relaxation activity of this material [42]. It is precisely the strong polarization losses distributed across multiple frequency bands that synergistically promote its multi-frequency, high-efficiency EMW absorption capability. This phenomenon can be attributed to the unique microstructure of the composite. The abundant 1D SiC nanowires, along with zero-dimensional (0D) SiC, Ce_5Si_4, and Pr_5Si_4 nanoparticles, collectively form a high density of diverse heterointerfaces (such as SiC/Ce_5Si_4, SiC/Pr_5Si_4, and Ce_5Si_4/Pr_5Si_4). These interfaces act as active centers for interfacial polarization, capable of generating intense polarization relaxation under an alternating electromagnetic field, thereby substantially enhancing the dielectric loss capability of the material [43].

To gain deeper insight into the polarization characteristics of the samples, Debye theory describing relaxation processes was employed. The relationship between ε' and ε'' can be expressed by the equation: $(\varepsilon' - \varepsilon_\infty)^2 + (\varepsilon'')^2 = (\varepsilon_s - \varepsilon_\infty)^2$ [44]. In this

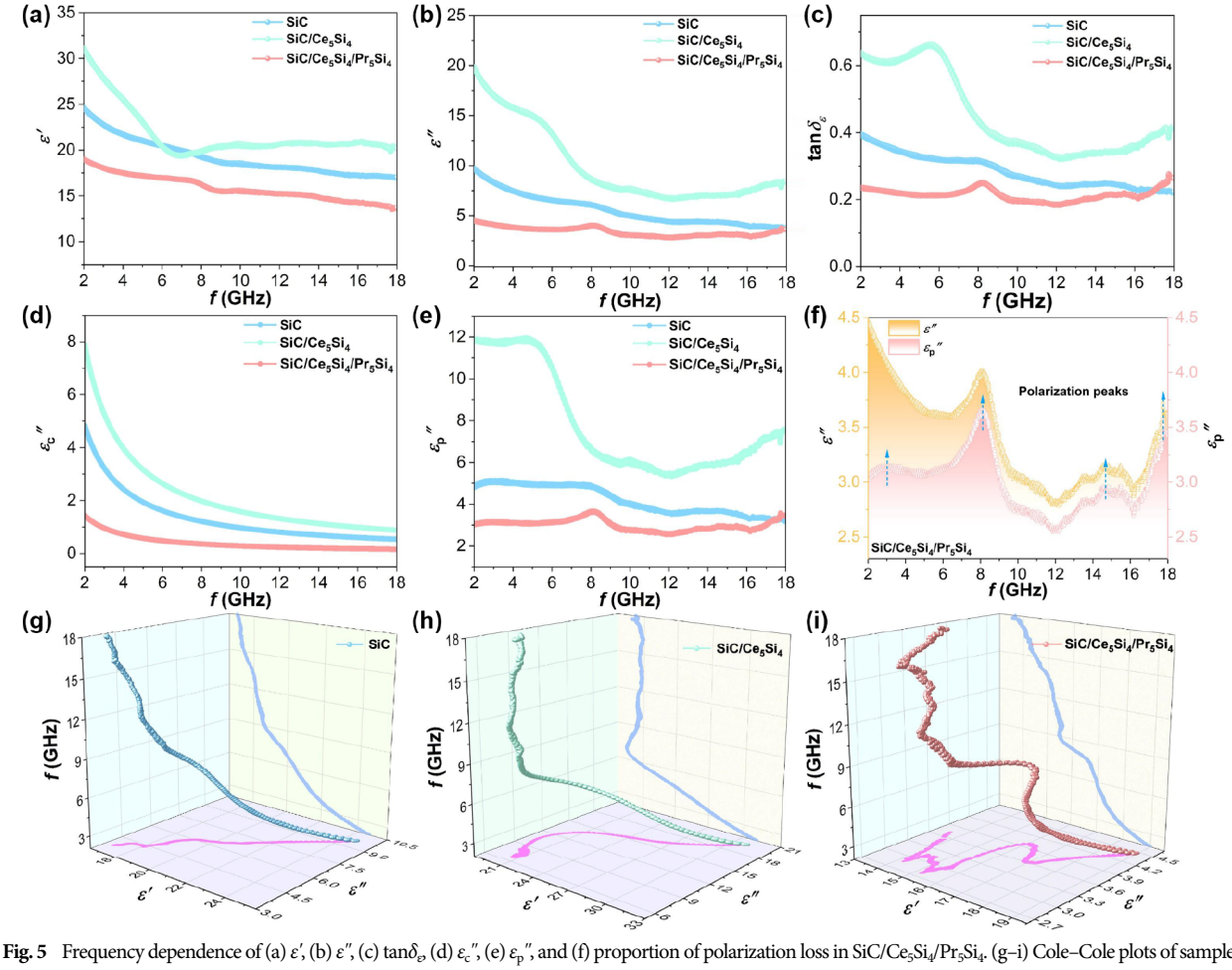

Fig. 5 Frequency dependence of (a) ε', (b) ε'', (c) $\tan\delta_e$, (d) ε_c'', (e) ε_p'', and (f) proportion of polarization loss in SiC/Ce_5Si_4/Pr_5Si_4. (g–i) Cole–Cole plots of samples.

representation, the presence of semicircles corresponds to polarization loss, while linear tails signify conduction loss. The number of semicircles is positively correlated with the strength of polarization loss, with a greater number indicating stronger polarization loss, whereas longer tails suggest more significant conduction loss [45]. As shown in Figs. 5(g)–5(i), the tails for each sample exhibit a linear characteristic, indicating the presence of conduction loss at low frequencies. In contrast, the $SiC/Ce_5Si_4/Pr_5Si_4$ sample (Fig. 5(i)) displays Cole–Cole semicircles across low, medium, and high frequencies, demonstrating the presence of multiple polarization relaxation processes [46]. This phenomenon further confirms that the introduction of the dual rare-earth elements Ce and Pr effectively enhances the dielectric polarization relaxation capability of the material, leading to high polarization loss, which is consistent with the polarization loss curves discussed above.

Achieving high-performance EMW absorption depends on two critical parameters: impedance matching (Z) and the attenuation constant (α) [47]. Here, the attenuation capability is primarily related to the electromagnetic loss mechanisms of the material, while the reflection behavior is determined by the degree of impedance matching. Impedance matching describes the effective alignment of impedance between free space and the material surface, expressed as $Z = (\mu_r/\varepsilon_r)^{1/2}\tanh|j2\pi fd(\mu_r\varepsilon_r)^{1/2}/c|$ [48]. On the Smith chart, the central point (1.0) represents the ideal matching state, where the input impedance (Z_{in}) of the material perfectly matches the impedance of free space, allowing EMW to enter the material without reflection [49]. Furthermore, the intersection points of the Z_{in} trajectory with the horizontal real axis correspond to resonance frequencies, where the imaginary part of the impedance is zero, indicating potential frequencies for strong absorption [50]. The blue area represents the region of favorable impedance matching, which extends outward from the center of the chart. Impedance trajectories located within this blue area, or closer to the center of the chart, indicate that the input impedance of the material is better matched to that of free space. Conversely, trajectories far from the blue area correspond to severe impedance mismatch. Figures 6(a)–6(c) show that the Z_{in} trajectory of the $SiC/Ce_5Si_4/Pr_5Si_4$ composite exhibits the broadest distribution within the blue region and lies closest to the chart center, indicating its optimal impedance matching characteristics. In contrast, the trajectory for SiC/Ce_5Si_4 only partially enters the blue region, with fewer data points inside, suggesting inferior matching performance. The trajectory for pure SiC, while intersecting the blue region, remains distant from the center, indicating that its impedance matching is unsatisfactory. These differences in impedance matching behavior are highly consistent with the measured EMW absorption performance of the three materials, further confirming the critical role of impedance matching in regulating absorption efficiency. Based on the quarter-wavelength theory, the relationship between the absorption peak frequency (f_m) and the matching thickness (t_m) satisfies [51]: t_m =

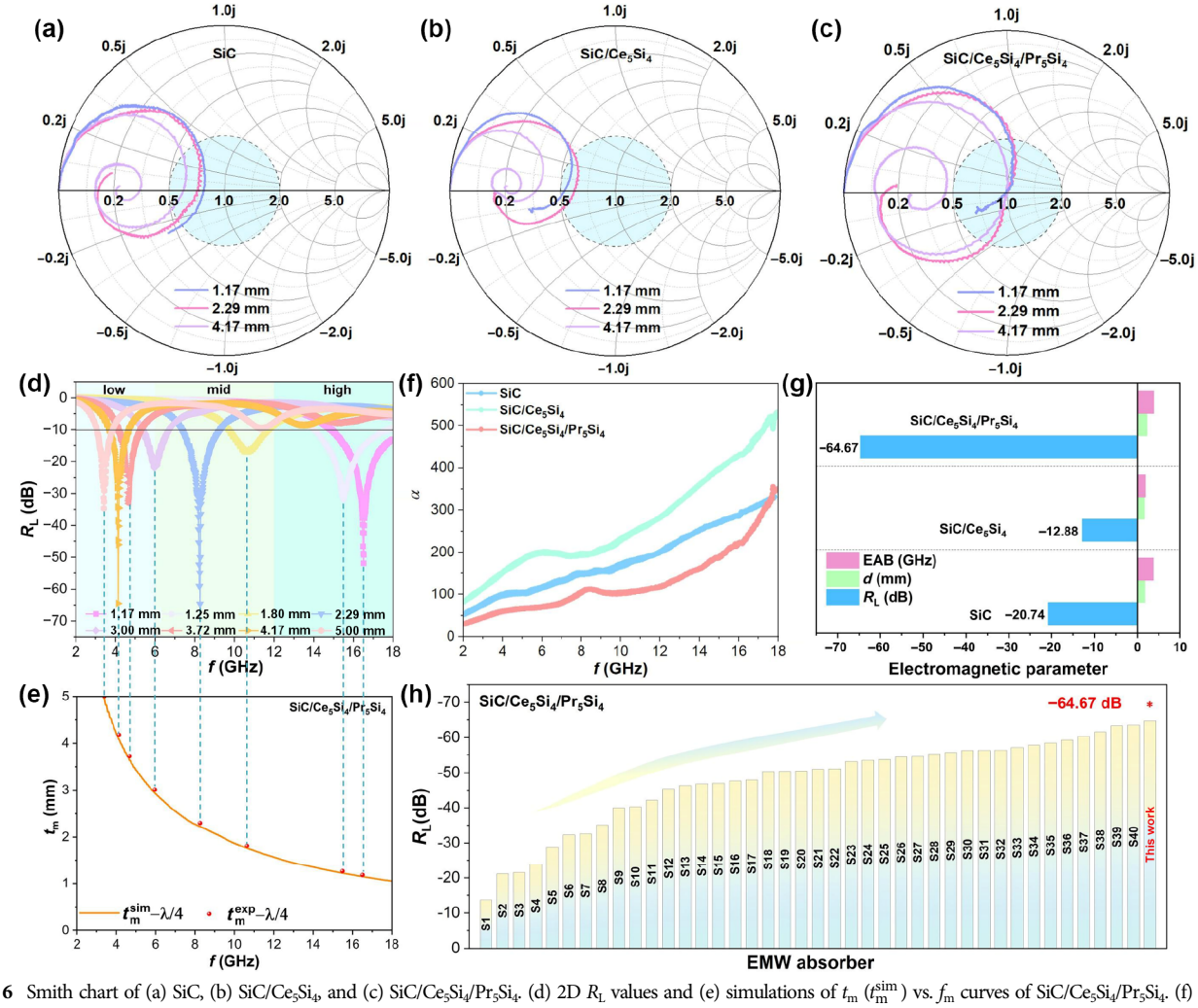

Fig. 6 Smith chart of (a) SiC, (b) SiC/Ce_5Si_4, and (c) $SiC/Ce_5Si_4/Pr_5Si_4$. (d) 2D R_L values and (e) simulations of t_m (t_m^{sim}) vs. f_m curves of $SiC/Ce_5Si_4/Pr_5Si_4$. (f) α and (g) electromagnetic behavior of samples. (h) Comparison of EMW absorption properties of $SiC/Ce_5Si_4/Pr_5Si_4$ with those of other SiC-based absorbers.

$nc/(4f_m(|\mu_r||\varepsilon_r|)^{1/2}$. As shown in Fig. 6(d), the SiC/Ce_5Si_4/Pr_5Si_4 composite exhibits strong absorption at 1.17 mm (16.51 GHz, Ku-band), 2.29 mm (8.24 GHz, X-band), and 4.17 mm (4.30 GHz, C-band). These thickness–frequency pairs agree well with the n = 1 quarter-wavelength matching condition (Fig. 6(e)), indicating that the absorption peaks arise from destructive interference within the material. The close match between the simulation and experiment validates this mechanism, demonstrating that the composite exhibits favorable impedance matching across different frequency bands.

The attenuation capability of a material can be evaluated by its attenuation constant (α), which is expressed as [52]: $\alpha = [(2)^{1/2}\pi f)/c]\ \{(\mu''\varepsilon'' - \mu'\varepsilon') + [(\mu''\varepsilon'' - \mu'\varepsilon')^2 + (\varepsilon'\mu'' + \varepsilon''\mu')^2]^{1/2}\}^{1/2}$. Theoretically, a higher α value indicates that EMW can be dissipated more effectively within the material. As shown in Fig. 6(f), although SiC and SiC/Ce_5Si_4 exhibit higher α values, their excessively high permittivity leads to significant impedance mismatch, which in turn limits their overall absorption performance. This result clearly demonstrates that achieving efficient EMW absorption relies not only on the material's intrinsic strong attenuation capability but also on the optimization of electromagnetic parameters to realize good impedance matching. Only through the synergistic effect of both can incident electromagnetic waves be maximally coupled into the material and effectively attenuated. Therefore, although the α value of SiC/Ce_5Si_4/Pr_5Si_4 is not the highest, it strikes an optimal balance between moderate attenuation capability and favorable impedance matching, thereby achieving the most exceptional multi-band EMW absorption performance (Fig. 6(g)). As presented in Fig. 6(h), a comparative analysis of EMW absorption performance

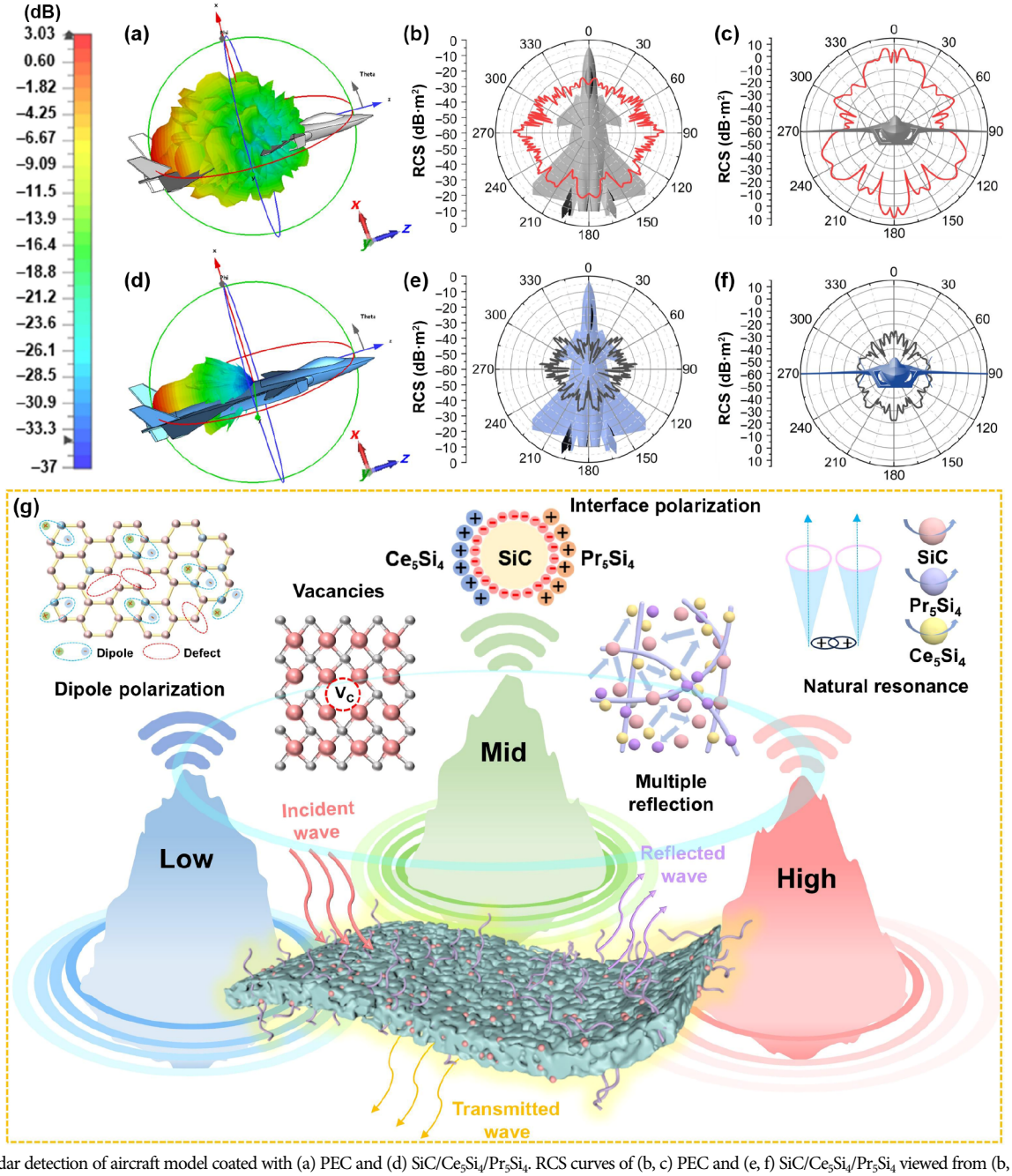

Fig. 7 Radar detection of aircraft model coated with (a) PEC and (d) SiC/Ce_5Si_4/Pr_5Si_4. RCS curves of (b, c) PEC and (e, f) SiC/Ce_5Si_4/Pr_5Si_4 viewed from (b, e) top and (c, f) front. Simulated at a frequency of 8.26 GHz and thickness of 2.29 mm. (g) Schematic diagram of EMW absorption mechanisms for SiC/Ce_5Si_4/Pr_5Si_4 heterostructures.

against other SiC-based EMW absorbers further confirms the superior characteristics of SiC/Ce_5Si_4/Pr_5Si_4 heterostructures.

To evaluate the potential of the SiC/Ce_5Si_4/Pr_5Si_4 composite for aircraft stealth design, this work used it as the research subject to comparatively analyze the RCS characteristics of this absorber configuration against a traditional metallic structure (benchmarked against a perfect electric conductor, PEC). Using CST Microwave Studio 2024 software, the RCS of both the PEC and SiC-based composite configurations was simulated under realistic far-field conditions. 3D scattered field distributions and azimuthal RCS patterns at typical frequencies were obtained for both configurations [53]. The simulation results indicate that the PEC configuration exhibits strong specular reflection in normal regions such as the nose and wing leading edges, with RCS peaks exceeding 5 dB·m^2 (Figs. 7(a)–7(c)). Furthermore, its azimuthal RCS polar plot contains multiple sharp, highly detectable peaks. In contrast, the SiC/Ce_5Si_4/Pr_5Si_4 configuration demonstrates a significant RCS reduction effect. The high-intensity reflection regions in its 3D scattered field are substantially reduced [54]. The RCS values remain below −20 dB·m^2 across all spatial orientations, with a more diffuse distribution of scattered energy (Figs. 7(d)–7(f)). The azimuthal RCS polar plot appears flatter overall, with notably lower and more uniformly distributed peaks. The simulation results confirm that this composite can significantly improve the spatial RCS distribution characteristics of an aircraft platform.

Based on the above analysis, we summarize the EMW absorption mechanism of the SiC/Ce_5Si_4/Pr_5Si_4 composite, as illustrated in Fig. 7(g). In this system, the introduction of dual rare-earth elements Ce and Pr promotes the *in situ* growth of SiC nanowires, collectively constructing a porous network skeleton. This structure not only provides physical space for multiple reflections and scattering of EMWs, thereby extending their propagation path inside the material and enhancing the gradual dissipation of energy, but also leads to charge accumulation at the heterointerfaces due to the significant differences in electrical conductivity and dielectric properties among the three phases (SiC, Ce_5Si_4, and Pr_5Si_4). This accumulation forms numerous interface dipoles. Under alternating electromagnetic field excitation, these dipoles cannot respond instantaneously to field variations due to interface resistance, resulting in pronounced interfacial polarization relaxation that effectively converts electromagnetic energy into thermal energy. Furthermore, Ce_5Si_4 and Pr_5Si_4, as typical rare-earth silicides, possess unpaired electrons within their crystal lattices, endowing the material with intrinsic magnetic properties. Owing to their distinct magnetocrystalline anisotropies, their natural resonance frequencies differ, exciting magnetic losses in specific frequency bands. Simultaneously, defects such as vacancies present in the composite serve as polarization centers, inducing local charge rearrangement and dipole moment imbalance, which trigger dipole polarization. Therefore, the SiC/Ce_5Si_4/Pr_5Si_4 composite achieves excellent EMW absorption performance across multiple frequency bands through the synergistic effects of various mechanisms, including interfacial polarization, dipole polarization, natural resonance, and multiple reflections and scattering.

4 Conclusions

In this work, a ternary SiC/Ce_5Si_4/Pr_5Si_4 heterostructure absorber based on dual rare-earth (Ce/Pr) modification was successfully constructed, featuring abundant heterogeneous interfaces and a porous structure. The experimental result indicates that the introduction of dual rare-earth elements not only optimizes impedance matching by modulating the complex permittivity but also establishes multiple interfaces between SiC and rare-earth silicides, inducing strong interfacial polarization relaxation, which serves as the dominant loss mechanism. Coupled with the multiple scattering effects promoted by the 3D network composed of 1D SiC nanowires and 0D nanoparticles, as well as the natural resonance arising from unpaired electrons in rare-earth silicides, this heterostructure achieves strong absorption below −50 dB in the C-band (4.3 GHz), X-band (8.24 GHz), and Ku-band (16.51 GHz), demonstrating exceptional multi-band EMW attenuation capability. RCS simulations further confirm its significant scattering reduction effect at typical radar frequencies. This work provides a new design concept and mechanistic insights for achieving multi-band and efficient EMW absorption through multi-element and multi-interface synergistic strategies.

Acknowledgements

This work was supported by the National Natural Science Foundation of China (No. 52562043), the Jiangxi Provincial Natural Science Foundation (No. 20244BAB28050), and the National University Students Innovation and Entrepreneurship Training Program (No. 202510408040X).

Availability of data and materials

The data that support the findings of this study are available from the corresponding author upon reasonable request.

Competing interests

The authors have no competing interests to declare that are relevant to the content of this article. The author Xiaojun Zeng is the Editorial Committee member of this journal.

Electronic Supplementary Material

Supporting Information is available in the online version of this article at https://doi.org/10.26599/JAC.2026.9221325.

References

[1] He MK, Hu JW, Yan H, *et al.* Shape anisotropic chain-like CoNi/polydimethylsiloxane composite films with excellent low-frequency microwave absorption and high thermal conductivity. *Adv Funct Mater* 2025, **35**: 2316691.

[2] Guan XM, Jiang MM, Shen ZH, *et al.* High-entropy interface engineering in multifunctional green fiber aerogels for coupled electromagnetic and waste-heat management. *Adv Funct Mater* 2026, **36**: 27596.

[3] Chen T, Yan YF, Liu SQ, *et al.* Lightweight and flexible fabric assembled by ANF/GMWCNT fibers for broadband electromagnetic wave absorption. *Adv Funct Mater* 2026, **36**: 28094.

[4] Zeng XJ, Peng XW, Liu Q, *et al.* BiM@NC (M = Fe, Co, Ni; NC = N-doped carbon) nanoplates confined in wood-derived carbon with excellent electromagnetic wave absorption performance. *Adv Funct Mater* 2026, **36**: 16772.

[5] Zhou L, Hu PF, Bai M, *et al.* Harnessing the electronic spin states of single atoms for precise electromagnetic modulation. *Adv Mater* 2025, **37**: 2418321.

[6] Gao BS, Yan YF, Zhang KL, *et al.* Ultralight broadband electromagnetic wave absorption enabled by interface-engineered two-layered periodic carbon fiber fabrics. *Adv Funct Mater* 2026, **36**: 32108.

[7] Huang J, Zeng XJ, Jiang X, *et al. In situ* construction of MXene derivatives and rare metal doping in nanofibers for multifunctional and ultrathin electromagnetic responses. *Adv Funct Mater* 2025, **35**: 10047.

[8] Hao B, Zhang Y, Si HX, *et al.* Multiscale design of dielectric

composites for enhanced microwave absorption performance at elevated temperatures. *Adv Funct Mater* 2025, **35**: 2423897.
[9] Li X, Wang XL, Li MH, *et al.* Built-in electric field enhancement strategy induced by cross-dimensional nano-heterointerface design for electromagnetic wave absorption. *Adv Funct Mater* 2025, **35**: 2407217.
[10] Zeng XJ, Deng XM, Yu ZJ, *et al.* Evolution of Fe single atom in SiOC ceramic fibers and their high-temperature and ultrathin electromagnetic wave absorption. *Adv Mater* 2026, **38**: 21533.
[11] Feng GH, Guo LX, Yu HY, *et al.* Uniting superior electromagnetic wave absorption with high thermal stability in bioinspired metamaterial by direct ink writing. *Adv Funct Mater* 2025, **35**: 2424499.
[12] Guo BL, Jiang YJ, Zhang YX, *et al.* Differentiated electromagnetic wave absorption enabled by load modulation of cross-dimensional SiC nanostructures. *Chem Eng J* 2025, **509**: 161364.
[13] Qian JJ, Ma DD, Zhou XL, *et al.* Synthesis of SiOC@C ceramic nanospheres with tunable electromagnetic wave absorption performance. *J Adv Ceram* 2024, **13**: 1394–1408.
[14] Hu Y, Ni DW, Chen BW, *et al.* Enhanced electromagnetic wave absorption in $(SiO_2–C)_f$/(CrZrHfNbTa)C–Si_3N_4–SiBCN composite by defect engineering and gradient permittivity modulation. *Compos Part B—Eng* 2025, **304**: 112668.
[15] Yang ZQ, Liang QQ, Qi XS, *et al.* Hollow engineering in CoNi@Air@C@MoS_2 multicomponent composites derived from bimetallic CoNi Prussian blue analogs for ultra-wide bandwidth and strong electromagnetic wave absorption. *J Mater Sci Technol* 2025, **212**: 35–43.
[16] Tan YN, Zeng XJ, Wu ZM, *et al.* Light/heavy rare earth-doped Mo-MXene: Excellent electromagnetic wave absorption based on dual-domain synergistic attenuation. *Adv Funct Mater* 2026, **36**: 25167.
[17] Cao YH, Zheng XR, Deng YD, *et al.* Comprehensive insight into electronic modulation of rare-earth elements for enhancing electrocatalytic performance of atomically dispersed materials. *Adv Funct Mater* 2025, **35**: 2423158.
[18] Zeng XJ, Zhao C, Jiang X, *et al.* Functional tailoring of multi-dimensional pure MXene nanostructures for significantly accelerated electromagnetic wave absorption. *Small* 2023, **19**: 2303393.
[19] Yan YF, Cheng ZY, Chen T, *et al.* Rational high-entropy doping strategy via modular*in situ*/post solvothermal doping integration for microwave absorption. *J Adv Ceram* 2025, **14**: 9221168.
[20] Xu YB, Hu WJ, Li YF, *et al.* Manipulating the cobalt species states to break the conversion–selectivity trade-off relationship for stable ethane dehydrogenation over ligand-free-synthesized Co@MFI catalysts. *ACS Catal* 2023, **13**: 1830–1847.
[21] Ma YR, Qu HQ, Wang WN, *et al.* Si/SiO_2@Graphene superstructures for high-performance lithium-ion batteries. *Adv Funct Mater* 2023, **33**: 2211648.
[22] Wu ZM, Huang J, Tan YN, *et al.* Transition/rare earth metal co-modified SiC for low-frequency and high-temperature electromagnetic response. *J Adv Ceram* 2025, **14**: 9221164.
[23] Ye J, Wang YJ, Ru HQ, *et al.* The morphology regulating effect of cobalt acetate on the vacuum carbothermal synthesis of β-SiC powder. *Ceram Int* 2023, **49**: 37253–37262.
[24] Ning Y, Jiang X, Huang J, *et al.* Trimetallic MOFs derived $NiFe_2O_4$/$MoNi_4$-NC Schottky heterojunctions with abundant defects and dielectric-magnetic coupling for electromagnetic response. *J Mater Sci Technol* 2025, **213**: 1–13.
[25] Zhang KL, Liu YH, Liu YN, *et al.* Tracking regulatory mechanism of trace Fe on graphene electromagnetic wave absorption. *Nano-Micro Lett* 2024, **16**: 66.
[26] Jiang X, Tan YN, Cheng SN, *et al.* Ce-4f/N double-doped Mo–MXene for regulating dielectric polarization response. *Nano Res* 2025, **18**: 94907512.
[27] Zhang H, Ouyang Q, Yu LL, *et al.* Transient and *in situ* growth of nanostructured SiC on carbon fibers toward highly durable catalysis. *Adv Funct Mater* 2023, **33**: 2301375.
[28] Wang JY, Zhou JT, Van Zalinge H, *et al.* Hollow spherical SiC@Ni composites towards the tunable wideband electromagnetic wave absorption. *Compos Part B—Eng* 2024, **276**: 111361.
[29] Deng M, Yang AJ, Ma J, *et al.* Enhanced catalytic performance of N-doped carbon sphere-supported Pd nanoparticles by secondary nitrogen source regulation for formic acid dehydrogenation. *ACS Appl Mater Inter* 2022, **14**: 18550–18560.
[30] Song LM, Zhang F, Chen YQ, *et al.* Multifunctional SiC@SiO_2 nanofiber aerogel with ultrabroadband electromagnetic wave absorption. *Nano-Micro Lett* 2022, **14**: 152.
[31] Liu A, Xu XS, Qiu H, *et al.* Bioinspired hollow heterostructure fillers for enhanced electromagnetic interference shielding in polyimide aerogels. *InfoMat* 2025, **7**: 70060.
[32] Zeng XJ, Deng XM, Huang J, *et al.* Bimetallic coupled porous SiC for multi-band and high-temperature electromagnetic wave response. *Nano Today* 2025, **63**: 102770.
[33] Huang B, Ye F, Deng JW, *et al.* Cross-scale structural engineering of MOF-derived Co_xNi_y@C nanorods with controllable electromagnetic response behavior for broadband electromagnetic wave absorption. *J Adv Ceram* 2026, **15**: 9221224.
[34] Wang ZQ, Wang SB, Fei H, *et al.* Atomic-scale elucidation of attenuation mechanisms underlying exceptional electromagnetic wave absorption of SiZrBCN ceramic nanocomposites. *J Adv Ceram* 2026, **15**: 9221221.
[35] Zeng XJ, Zhao C, Yin YC, *et al.* Construction of $NiCo_2O_4$ nanosheets-covered $Ti_3C_2T_x$ MXene heterostructure for remarkable electromagnetic microwave absorption. *Carbon* 2022, **193**: 26–34.
[36] Tang SW, Cheng SA, Yu C, *et al.* Impedance-matchable 3D MXene sponge/NiFe@NC heterostructure with tunable pores for efficient electromagnetic wave absorption and thermal resistance. *Sci China Mater* 2026, **69**: 1706–1718.
[37] Li MH, Song XR, Xue JM, *et al.* Construction of hollow carbon nanofibers with graphene nanorods as nano-antennas for lower-frequency microwave absorption. *ACS Appl Mater Inter* 2023, **15**: 31720–31728.
[38] Zeng XJ, Peng XW, Ning Y, *et al.* 3D multifunctional porous pine carbon aerogels coupled with highly dispersed CoFe nanoparticles for robust electromagnetic wave response. *J Mater Sci Technol* 2024, **192**: 6–18.
[39] Cheng YH, Liu X, Ren JW, *et al.* Component-based modulation engineering to improve magnetoelectric coupling for self-anticorrosion broadband absorption. *Carbon* 2025, **239**: 120325.
[40] Wang YQ, Liu CY, Qu HC, *et al.* Enhanced low-frequency microwave absorption and corrosion resistance of FeSiAl using low-melting-point glass phase coatings. *Rare Metals* 2026, **45**: 70069.
[41] Zhang K, Liu Y, Li X, *et al.* All-dielectric ultra-broadband microwave absorbing aerogel with optimized dielectric dispersion via dielectric relaxation time regulation. *Adv Mater* 2025, **37**: 2506386.
[42] Shao GF, Yang YH, Jia SW, *et al.* Covalent organic framework-amplified polarization loss in ultralight Schottky heterojunction aerogels for low-frequency electromagnetic wave absorption. *Adv Funct Mater* 2026, **36**: 16078.
[43] Zeng XJ, Nie TL, Zhao C, *et al. In situ* exsolution-prepared solid-solution-type sulfides with intracrystal polarization for efficient and selective absorption of low-frequency electromagnetic wave. *Adv Sci* 2024, **11**: 2403723.
[44] Wang JL, Qu HC, Ye XY, *et al.* Electronic structure and absorption mechanism of Fe-doped $Y_{0.9}Sr_{0.1}CoO_3$ perovskite microwave absorbers. *J Adv Ceram* 2025, **14**: 9221191.
[45] Chang Q, Xie ZJ, Chen G, *et al.* Enhancement in conduction loss induced by morphology engineering for excellent electromagnetic wave absorption. *J Materiomics* 2025, **11**: 100927.
[46] Huang J, Chen YY, Xie NH, *et al.* Rare earth-induced multiscale dual-phase dielectric hierarchical materials enabled lightweight and broadband electromagnetic response. *Carbon* 2026, **246**: 120896.
[47] Yang CW, Li KW, Hu MG, *et al.* Flexible ZrO_2/ZrB_2/C nanofiber felt

with enhanced microwave absorption and ultralow thermal conductivity. *J Materiomics* 2025, **11**: 100988.
[48] Wu ZM, Huang J, Zeng XJ. Dual magnetic particles modified carbon nanosheets in CoFe/Co@NC heterostructure for efficient electromagnetic synergy. *Soft Sci* 2024, **4**: 42.
[49] Fang X, Huang YQ, Lin YB, *et al.* Manipulating terminal bonds of $Ti_3C_2T_x$ MXene for highly efficient microwave absorption and photothermal conversion. *Rare Metals* 2026, **45**: 70219.
[50] Niu QQ, Huang Y, Huang HJ, *et al.* A flexible and repairable ultra-broadband electromagnetic wave absorber by liquid–liquid phase separation strategy. *Adv Mater* 2025, **37**: 10139.
[51] Zeng XJ, Jiang X, Ning Y, *et al.* Constructing built-in electric fields with semiconductor junctions and Schottky junctions based on Mo–MXene/Mo–metal sulfides for electromagnetic response. *Nano-Micro Lett* 2024, **16**: 213.
[52] Wu P, Wang J, Li JY, *et al.* Pseudo-binary composite of Sr_2TiMoO_6–Al_2O_3 as a novel microwave absorbing material. *Rare Metals* 2025, **44**: 503–514.
[53] Lin YB, Yu KX, Zhong B, *et al.* Liquid metal modified hexagonal boron nitride flakes for efficient electromagnetic wave absorption and thermal management. *J Adv Ceram* 2025, **14**: 9221208.
[54] An Q, Li DW, Liao WH, *et al.* A novel ultra-wideband electromagnetic-wave-absorbing metastructure inspired by bionic gyroid structures. *Adv Mater* 2023, **35**: 2300659.